Journal of Materials Chemistry A

ROYAL SOCIETY OF CHEMISTRY

PAPER

View Article Online
View Journal | View Issue

Cite this: J. Mater. Chem. A, 2025, 13, 15257

Organic shell engineering of $CsPbBr_3$ perovskite quantum dots for efficient textile-based photodetectors†

Jan Nawrocki, [a] Vishnu Anilkumar, [a] Guobin Jia,[b] Apurba Mahapatra, *[a] Piotr Bernatowicz, [a] Jan Dellith,[b] Gayatri,[c] Mateusz Raczyński, [c] Arka Karmakar, [c] Pankaj Yadav,[d] Seckin Akin,[e] Benjamin Dietzek-Ivanšić,[b] Maciej R. Molas, [c] Jonathan Plentz [b] and Daniel Prochowicz *[a]

Lead halide perovskite quantum dots (QDs) have emerged as next-generation materials for photodetectors (PDs). It is well known that conventional alkyl long-chain ligands show weak binding on the surface of the QD core, leading to low stability and poor charge transfer. Herein, we explore the effect of partial replacing of alkyl long-chain ligands with aromatic short-chain ligands, namely phenylethylamine (PEA) and *trans*-cinnamic acid (TCA), on the performance of $CsPbBr_3$ QDs-based PD deposited on textile. The planar-type PDs with optimum PEA (L-type) and TCA (X-type) ligand doping concentration show improved performance compared to the control device due to the combined effect of enhanced conductivity and photoluminescence lifetime, lower surface defect centres, and reduced non-radiative recombination. Notably, PEA-treated $CsPbBr_3$ QDs-based PD shows the best photodetection properties of blue light (448 nm) at 10 V with a peak responsivity of 149 mA W^{-1} and EQE of 41.3%, which is almost 20 times higher than those of the control device and 3 times higher than the TCA-treated $CsPbBr_3$ QDs based device. In addition, this device reveals excellent mechanical and operational stability. These results pave the way for designing flexible and wearable perovskite QDs-based optoelectronic devices, which may find potential applications in future optoelectronic devices.

Received 2nd January 2025
Accepted 17th April 2025

DOI: 10.1039/d5ta00046g

rsc.li/materials-a

1. Introduction

Photodetectors (PDs), whose working principle is based on the photoelectric phenomenon, are devices capable of converting incident photons into a current response by generating electron and hole pairs. According to the device structure and working principle, PDs can be classified into photoconductors, phototransistors, and photodiodes.[1] In the digital age, the demand for PDs is growing significantly, and the main areas of exploration for new technologies are focused on X-ray detection,[2] infrared sensing,[3] health monitoring sensors,[4,5] image sensing,[6,7] optical communication,[8] and wearable electronics.[9] In turn, PDs on textiles open up completely new applications in the fields of well-being, safety, energy harvesting, monitoring of health and environmental conditions.[10,11] Recently, lead halide perovskites (LHPs) have emerged as promising semiconducting materials for photodetection applications because of their outstanding properties such as a tunable bandgap, long carrier lifetimes and high diffusion length.[12] To date, different forms of LHPs including single crystals,[13–18] bulk polycrystalline films[19–21] as well as quantum dots (QDs) films[22–25] have been applied for the formation of photodetector devices. Among them, LHP QDs became the subject of intensive research in photodetection owing to their tunable composition, high photoluminescence quantum yield, and multiple exciton generation mechanism.[26] However, the high stability and performance of LHP QD-based PDs are still the main challenges.

The important components of LHP QDs are organic capping ligands, which play an essential role in modulating stability and optoelectronic properties including charge carrier transport.[27] The most widely used capping ligand for colloidal perovskite QDs is the pair of oleic acid and oleylamine, whose long-chain insulating character hinder the improvement of device performance.[28] To address this issue, Zhou *et al.* proposed the use of mesoporous TiO_2 (mp-TiO_2), which acts as a scaffold material capable of extracting charge carriers from the QDs.[29] The PD

[a]Institute of Physical Chemistry, Polish Academy of Sciences, Kasprzaka 44/52, 01-224 Warsaw, Poland. E-mail: amahapatra@ichf.edu.pl; dprochowicz@ichf.edu.pl
[b]Leibniz Institute of Photonic Technology (Leibniz IPHT), Albert-Einstein-Strasse 9, 07745 Jena, Germany
[c]Institute of Experimental Physics, Faculty of Physics, University of Warsaw, 02-093 Warsaw, Poland
[d]Department of Solar Energy, School of Energy Technology, Pandit Deendayal Energy University, Gandhinagar-382 007, Gujarat, India
[e]Department of Metallurgical and Materials Engineering, Necmettin Erbakan University, Konya, 42090, Turkey

† Electronic supplementary information (ESI) available. See DOI: https://doi.org/10.1039/d5ta00046g

device based on a bilayer composite mp-TiO_2/$CsPbBr_3$ QDs exhibits a significantly enhanced performance than the pure QDs-based device, showing three orders of magnitude higher on/off ratio and a 44-fold increase in responsivity. Similarly, the hybridization of LHP QDs with graphene appears as a convenient method to create high-performance PDs by promoting the separation of photoinduced electron–hole pairs.[30–32]

Another approach for the development of efficient LHP QDs-based devices is surface ligand-shell engineering. Particularly, the introduction of short-chain ligands containing functional groups was reported not only to improve the charge carrier transport but also to maintain the colloidal stability and passivate diverse defect sites of LHP QDs.[27] For example, Vickers *et al.* demonstrated that the incorporation of short conductive aromatic ligands such as benzoic acid and benzylamine on the surface of QDs facilitates charge transport due to efficient surface passivation of defect regions and delocalization of the electronic wave function from the QDs.[33] The organic shell modification with short-chain aromatic ligands was also discussed by Wang *et al.*[34] It was demonstrated that the addition of benzyl iodide not only passivates the surface defects but also realizes p-doping character, which shifts the positions of the valence band and significantly reduces the hole injection barrier in devices. In another work, Yan *et al.* reported on an *in situ* polymerization method of 3,4-ethylenedioxythiophene on a surface of $CsPbBr_3$ QDs under the photocurrent of the PD.[35] The introduction of an aromatic polymeric shell to cross-link the LHP QDs enhances the conductivity and allows for high moisture resistance of the device. These studies and many others[36–39] have proven that surface treatment engineering with various ligands plays a significant role in the LHP QDs colloidal stability, morphology and photoluminescence properties. On the other hand, the effect of different ligand types on the performance of PDs based on colloidal LHP QDs has been little explored to date.[25] It is well known that surface ligands can be defined as types L, X, or Z according to coordination chemistry.[40] Typically, X-type ligands donate one electron to form metal–ligand bond, while L-type ligands are neutral two-electron donors with a lone electron pair that coordinates with surface cations. Therefore, we posit to investigate the influence of short-chain capping ligands, chosen judiciously with similar size but varied type (X- or L-type) and functionality, on the photodetection figure of merits of $CsPbBr_3$ QDs-based devices.

In this study, we selected aromatic short-chain ligands such as phenethylamine (PEA) and *trans*-cinnamic acid (TCA) as typical L- and X-type ligands to modify $CsPbBr_3$ QDs shell, respectively. First, we synthesized $CsPbBr_3$ QDs whose organic shells were modified with PEA and TCA capping ligands using a ligand-assisted reprecipitation (LARP) technique. The resulting materials were structurally and spectroscopically characterized, and their morphology was determined by transmission electron microscopy (TEM). In addition, we discussed the composition and interaction of the organic shell with the QD core using ^{1}H NMR and ^{1}H NOESY NMR spectroscopies. Then, after optimizing the ligand concentration on the surface of QDs, we prepared and fully characterized the photoconductor-type PD deposited on a flexible textile substrate. Our results reveal that the PEA-treated $CsPbBr_3$ QDs film gives rise to better charge transport with improved PL lifetime, lower surface defect centres, and reduced non-radiative recombination compared to the reference film. However, despite the enhanced conductivity in the TCA-treated $CsPbBr_3$ QDs film, the higher level of non-radiative recombination, defects, and second-order charge recombination restricts its performance compared to the PEA-treated $CsPbBr_3$ QDs-based PD. The PEA-treated $CsPbBr_3$ QDs-based PD shows the best photodetection properties of blue light at 10 V with a peak responsivity of 149 mA W^{-1} and EQE of 41.3%, which is almost 20 times higher than those of the control device as well as much higher than the all other reported $CsPbBr_3$ QDs based photoconductor. Finally, the flexibility and long-term operational and environmental stability tests prove the excellent stability of $CsPbBr_3$ QDs-based PD.

2. Results and discussion

A well-developed facile ligand-assisted re-precipitation (LARP) technique was used to synthesize all inorganic $CsPbBr_3$ QDs under ambient conditions (for synthesis details, see the Experimental section).[41] Briefly, we used a branched-chain didodecyldimethylammonium bromide (DDAB) together with *n*-octanoic acid (OA) to prepare a reference $CsPbBr_3$ QDs according to the recently published procedure.[42] Since the exchange of alkyl long-chain ligands into aromatic short-chain ones would lead to rapid aggregation of QDs and therefore inability to thin film solution processing, we decided to investigate the effect of partial ligand exchange on the optoelectronic properties of $CsPbBr_3$ QDs, maintaining their good solubility in toluene. The ligand exchange procedure involves the addition of various amounts of PEA and TCA ligands to the suspension of freshly prepared $CsPbBr_3$ QDs in toluene, forming the modified $CsPbBr_3$ QDs (hereafter abbreviated as PEA QDs and TCA QDs, respectively). Scheme 1 shows the schematic illustration of the synthesized QDs with their chemical compositions.

The sizes and distribution of QDs were analyzed by TEM as shown in Fig. 1a. It was found that the shape of QDs reveals no obvious changes before and after modification, showing a monodisperse cubic shape. However, we observed that the size of the pristine $CsPbBr_3$ QDs slightly decreases upon introduction of PEA or TCA ligands (Fig. S1 and Table S1†). Next, XRD measurements were conducted to evaluate the effect of used ligands on the crystal structure of precipitated QDs. As shown in Fig. 1b, all samples prepared by drop-casting of QDs on the glass substrates exhibit similar peaks corresponding to (100), (110), (200), (210), (211) and (220) diffraction planes, which indicate a retention of cubic perovskite crystal structure.[43] In addition, the diffraction peak at ~37.7° corresponds to the (211) crystal plane of the perovskite structure did not show any significant shift, and has almost the same full width at half maxima (FWHM) value after the ligand exchange with PEA and TCA, which confirms that the crystal structure of CsPbBr3 QDs remained unchanged (Fig. S2†). The synthesized $CsPbBr_3$ QD solutions possess strong green emission, as presented in Fig. S3.† Fig. S4† demonstrates the PL spectra of the obtained

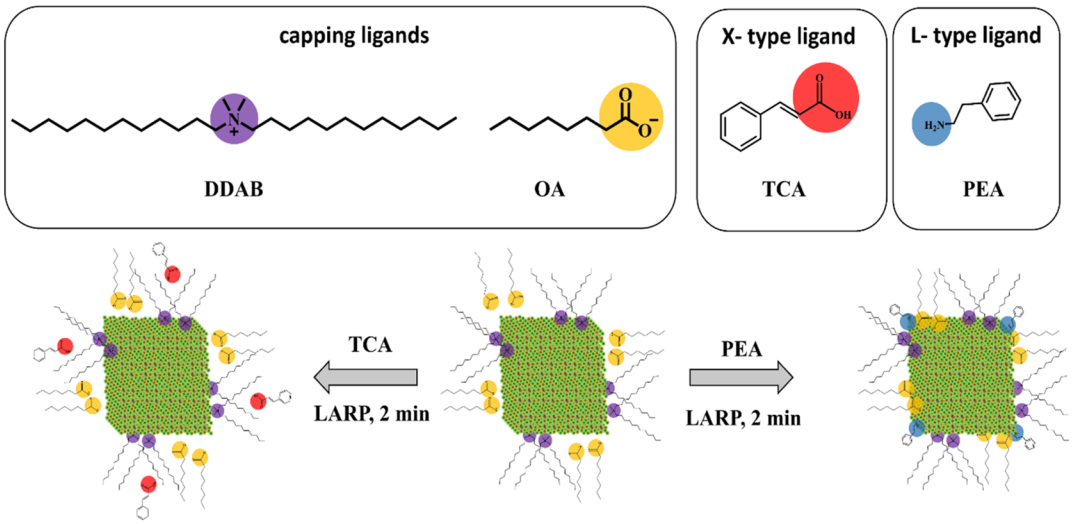

Scheme 1 Schematic illustration of the $CsPbBr_3$ QDs synthesis.

QDs in hexane solution, indicating the narrow emission peak with the maximum located at 516 nm for the reference sample, and 513 and 515 nm for the PEA- and TCA-treated $CsPbBr_3$ QDs, respectively.

The used organic ligands could also affect the band energy structure of the QD samples, which was investigated by ultraviolet-visible (UV-vis) absorption spectroscopy and ultraviolet photoelectron spectroscopy (UPS). UV-vis absorption

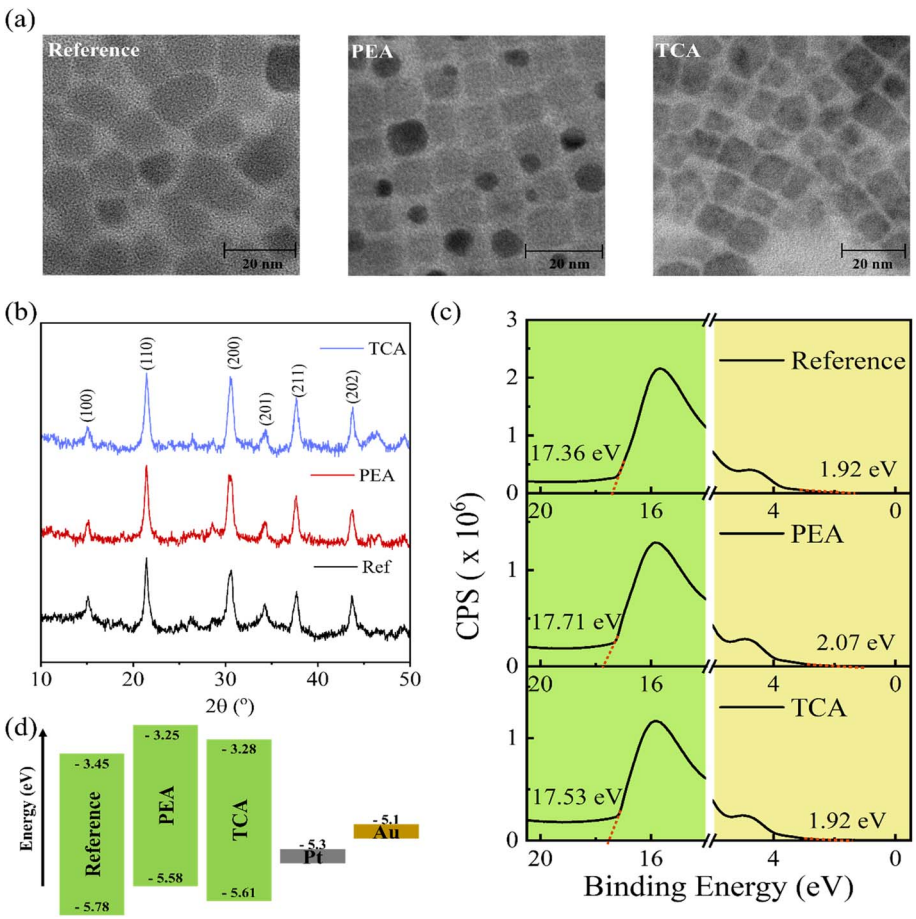

Fig. 1 (a) TEM micrographs; (b) XRD patterns; (c) UPS spectra and (d) representation of the energy-level diagram of the reference, PEA and TCA modified $CsPbBr_3$ QDs with respect to the vacuum level (E_{VAC}).

spectra collected for the reference and modified QDs exhibit almost similar onsets at ~504 nm (Fig. S5†). The optical band gap calculated by Tauc plot for the reference sample shows a value 2.33 eV, which is consistent with the literature.[42] In turn, band gaps for PEA- and TCA-treated $CsPbBr_3$ QDs slightly increases to 2.34 eV. The analysis of UPS results for the reference $CsPbBr_3$ QD film provides a valence band maximum (VBM) of −5.78 eV (Fig. 1c). In turn, the VBM of the TCA and PEA-modified $CsPbBr_3$ QD film is estimated to be equal to −5.61 and −5.58 eV, respectively. As shown in Fig. 1d, the VBM of PEA modified $CsPbBr_3$ QD sample shows a more favourable band alignment match with the work function of Pt metal electrode, which should facilitate easier hole extraction under illumination and consequently enhance the device performance.

The presence and type of the binding motifs of capping ligands with the perovskite were analyzed by ^{1}H nuclear magnetic resonance (NMR). For the calculation of the ratio between capping ligands, see Fig. S6–S8 and ESI Note 1.† In ^{1}H NOESY NMR spectra of all the QD samples the signals of groups bonded to nitrogen atom of DDABr reveal cross-peaks to the neighbouring CH_2 groups whose phase is the same as the phase of NOESY diagonal (Fig. S9–S11†). This means that the longitudinal dipole–dipole relaxation between these groups is in the regime where the zero-quantum relaxation prevails over the double-quantum one. This happens when $\omega\tau_c \gg 1$, where ω is Larmor frequency and τ_c is the rotational correlation time of the molecule. In our case of Larmor frequency of 500 MHz, the correlation time must then be much larger than 3^{-10} s. For a small molecule of weight about 400 g mol^{-1} such a slow reorientation may in non-viscous solvent only occur when it is attached to larger object. Therefore, it is likely that in the case of all QDs, the DDABr molecules strongly interact with the QDs, possibly substituting Cs sites on the surface.[44] In the ^{1}H NOESY spectrum of control $CsPbBr_3$ QDs, in the region where the cross-peaks between CH_3 and CH_2 groups appear, there is only one cross-peak whose phase is the same as NOESY diagonal. It is obviously related to the slowly tumbling DDABr molecules immobilized on the QD surface. The other cross-peaks between strongly overlapping CH_2 and CH_3 groups are of opposite phase. This suggests that the OA molecules are in the fast reorientation regime, *i.e.* they are not attached to the QD surface or attached very weakly. The picture is similar in the TCA-treated $CsPbBr_3$ QDs where DDABr seems to be attached to the QD surface, while OA is not. The resonances of TCA do not reveal NOESY cross-peaks, neither to DDABr nor to OA signals, so that it seems that TCA freely tumbles in the solution. Consequently, carboxylate ions do not bind to the QD, but rather neutralize charge on the surface by formation of equilibrium with the DDA ions. In the ^{1}H NMR spectrum of PEA-treated $CsPbBr_3$ QDs all the signals of PEA and the signals of CH_2 and CH_3 groups neighbouring to the nitrogen atom of DDABr, appear as very broad (half-width-at-half-height *ca.* 300 Hz at magnetic field of 11.7 T) humps. Since the widths of the latter scale linearly with the induction of the magnetic field, they appear to originate from an amorphous solid phase, and their large widths are due to the distribution of isotropic chemical shifts. In the ^{1}H NOESY spectrum there are cross-peaks of the same phase as diagonal peaks, linking the common broad signal of exchangeable protons (COOH and NH_2) at 0.8 ppm, PEA signals, DDABr signals and OA signals. It seems then that the core of PEA-treated $CsPbBr_3$ QDs is covered with the solid phase consisting of DDABr and PEA. The OA, although interacts with the QD surface strongly enough to reveal intense cross-peaks in the NOESY spectrum, shows relatively narrow NMR signals. This suggests that OA is not an ingredient of the amorphous solid constituted by DDABr and PEA on the QD surface but has rotational mobility which allows for efficient chemical shift tensor averaging to the isotropic line.

Since $CsPbBr_3$ QDs have been demonstrated as a promising material for photodetection applications,[25,45,46] we sought to investigate how the new ligand shell affects the device performance. Flexible PDs have received increasing attention due to their promising applications in various fields. Here, we used a glass fiber fabric as a flexible and textile substrate for the photodetectors layer system (Fig. S12†). The glass fiber fabric is coated with polytetrafluoroethylene (PTFE) with thicknesses between 70 μm and 250 μm.[47] First, we analyze the effect of gold (Au) and platinum (Pt) electrodes on the transient photoresponse of the control $CsPbBr_3$ QDs to select proper metal electrode for deposition.[16] The experiments were conducted at a fixed bias of 10 V and under a blue LED (λ = 448 nm) light pulse with irradiance power densities ranging from 0.1 to 50 mW cm^{-2}. The schematic of the studied PD architecture is shown in Fig. 2a. From Fig. 2b, we can observe that the control sample with Pt electrodes generates almost ~10 times higher photocurrent than the Au-based counterpart, which suggests its superior charge transfer due better Schottky barrier height (SBH) alignment with the $CsPbBr_3$ QDs (Fig. 1d). Therefore, we chose the Pt electrode for further fabrication and characterization of modified $CsPbBr_3$ QDs-based PDs.

Next, we investigate the effect of PEA at various doping concentrations (35, 70, 100 and 150 μL) on the photodetection performance of $CsPbBr_3$ QDs-based PD. Fig. S13† shows TEM images of $CsPbBr_3$ QDs with different concentrations of PEA. As seen, the size of $CsPbBr_3$ QDs decreases with increasing the concentration up to 100 μL (Table S1†). The dark current (I_d) is an essential parameter for the characterization of PD. Fig. 2c shows that the reference $CsPbBr_3$ QDs-based device exhibits the lowest I_d, which increases with increasing the PEA ligand amount up to 100 μL and drops for PEA = 150 μL but it is still higher than the I_d of the reference $CsPbBr_3$ QDs based PD. The enhanced I_d upon the addition of PEA could be explained by the improved conductivity of the $CsPbBr_3$ QDs film. The average conductivity of the control and PEA-based $CsPbBr_3$ QDs films is shown in Table S2.† As expected, PEA-modified $CsPbBr_3$ QDs films shows higher conductivity as compared to the control sample likely due to the insertion of the π-conjugation benzene ring and the ligand shortening by partially replacing the insulating ligands with PEA, which helps to improve electronic coupling between the ligands and QDs.[48] The reduced conductivity of the $CsPbBr_3$ QDs with 150 μL PEA could be due to the possible formation of an insulating layer created by higher ligand concentration. Further we collected and compared the PD performance for the reference and PEA-modified all $CsPbBr_3$

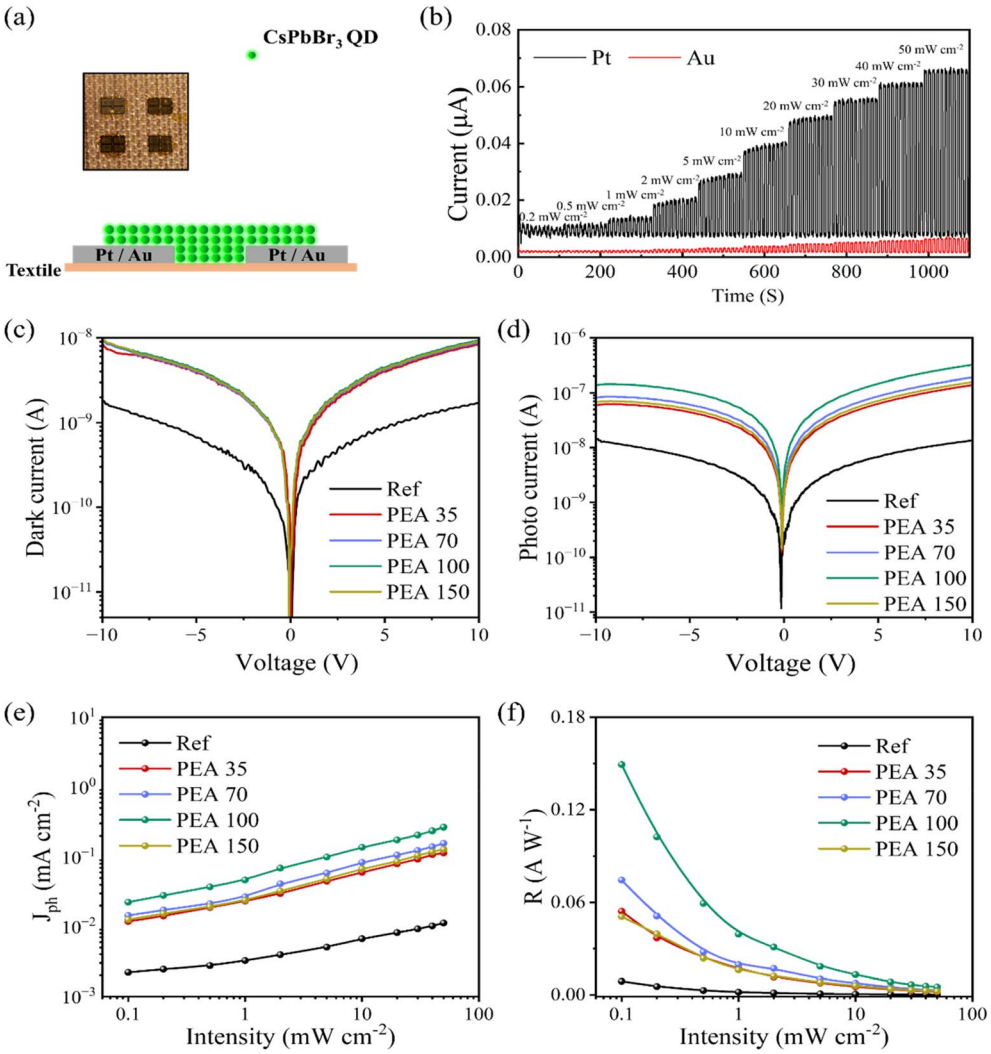

Fig. 2 (a) Schematic of the $CsPbBr_3$ QDs-based PD. The 200 μm metal electrode distance was chosen to avoid short circuit caused by textile roughness and flexibility test (inset: top view of the device). (b) Intensity-dependent transient photoresponses of the fabricated $CsPbBr_3$ QDs-based PD with Pt and Au electrode. *I–V* characteristics of the fabricated $CsPbBr_3$ QDs based PDs with different PEA concentrations under (c) dark and (d) 50 mW cm^{-2} blue light illumination. (e) Photocurrent density and (f) responsivity of the fabricated $CsPbBr_3$ QDs-based PDs with different PEA concentrations.

QDs under blue LED (λ = 448 nm) light irradiation. Typical logarithmic current–voltage (*I–V*) curves under 50 mW cm^{-2} blue light irradiance are shown in Fig. 2d. As seen, the photocurrent (I_{ph}) increases with increasing the bias, and the $CsPbBr_3$ QDs with 100 μL PEA exhibits the highest I_{ph} as compared to the other devices. This could be ascribed to the enhanced conductivity and lower amount of traps, which increase the photogenerated charge extraction under external bias. To shed more light on the effect of PEA concentration on the traps and charge generation of $CsPbBr_3$ QDs films, we analyzed their PL and time-resolved PL (TRPL) spectra at room temperature by fitting with a tri-exponential decay function, where the relatively fast (τ_1), intermediate (τ_2), and slow (τ_3) decay components are related to the charge transfer, radiative recombination, and nonradiative recombination of free charge carriers, respectively (Fig. S14 and Table S3†).[49] The PL intensity increases with increasing the amount of PEA to 100 μL and drops for film with 150 μL PEA. The average PL lifetime of the $CsPbBr_3$ QDs film with 100 μL PEA equals 20.53 ns, which is longer than that of the control film (16.48 ns). The difference between the average lifetimes for the films with different PEA concentrations is not clearly distinguishable. However, when we combine TRPL and PL data and extracted the comparison of radiative rate, we found that the $CsPbBr_3$ QDs film with 100 μL PEA shows almost four-times higher radiative rate compared to the control film. The higher radiative recombination value in the $CsPbBr_3$ QDs film with 100 μL PEA allows the overall recombination process to be proportionately less dominated by non-radiative recombination processes, which suggest lower surface defect centers in PEA-modified $CsPbBr_3$ QDs films.[50] These results indicate the reduction in non-radiative recombination after PEA modification and reconfirmed the presence of lowest defects in the $CsPbBr_3$ QDs film with 100 μL PEA.[51]

To get more information about the effect of PEA concentration on the recombination and PD performance, we measured the transient photoresponses of all the PDs at 10 V constant bias and under blue light intensity ranging from 0.1 to 50 mW cm^{-2} (Fig. S15†). Fig. 2e shows the logarithmic plot of J_{ph} as a function of the irradiation intensity under a constant bias of 10 V for all the devices. To reveal the recombination-dependent relationship between the photocurrent and irradiation power, we fitted these results with a power law ($J_{ph} \propto P^{\beta}$, where P is the irradiation power and β is the recombination under illumination).[18] A nonunity exponent of β ($0 < \beta < 1$) indicates existence of complex processes of carrier generation, charge trapping, and charge recombination. However, the β exponent value are significantly less than 1 which suggests the domination of Shockley–Read–Hall recombination (trap-assisted recombination) in our $CsPbBr_3$ QDs-based PD. The maximum value of the β exponent increases to 0.41 for the 100 μL PEA-modified $CsPbBr_3$ QDs-based PD compared to the control device (β = 0.27), which indicates lower recombination and better charge collection under external bias. The parameters of the photodetector performance (responsivity (R), external quantum efficiency (EQE), and specific detectivity (D^*)) of the fabricated PDs were calculated using eqn (S1)–(S4),† respectively (see ESI Note 2,†). As expected, PD based on $CsPbBr_3$ QDs with 100 μL PEA exhibits the highest values of R, D^* and EQE compared to other devices (Fig. 2f and S16†).

In order to probe ligand-type mediated PD performance, we have compared devices based on $CsPbBr_3$ QDs with 100 μL (0.81 mmol) PEA (L-type) and 120 mg (0.81 mmol) TCA (X-type). As can be seen in Fig. 3a, there is a slight increase in the dark current for the TCA-treated PD compared to the PEA treated device, which can be attributed to the higher conductivity of the TCA-treated $CsPbBr_3$ QDs film (Table S2†). The PL intensity of the TCA-modified $CsPbBr_3$ QDs film is almost 5 times lower than the PL intensity of the PEA treated film (Fig. S17†), which indicates higher non-radiative recombination and higher defects in the

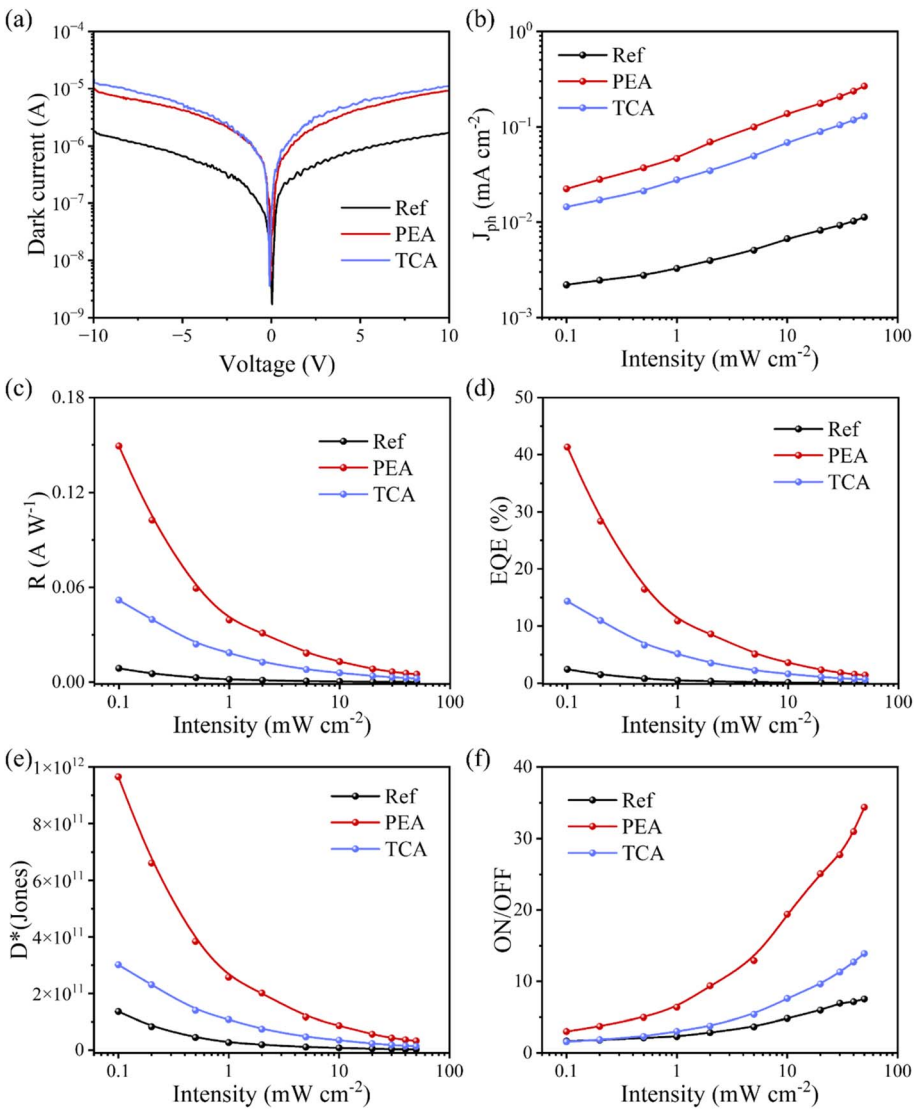

Fig. 3 (a) I–V characteristics of the fabricated $CsPbBr_3$ QDs-based PDs under dark. (b) Photocurrent density, (c) responsivity, (d) EQE, (e) specific detectivity and (f) on/off ratio of the fabricated $CsPbBr_3$ QDs-based PDs.

Table 1 Comparison of photodetector parameters of reported $CsPbBr_3$ QDs based photodetector with our work

Device	λ_{exc}	Bias (V)	R (A/W)	D^* (Jones)	EQE (%)	On/off	Reference
Au/$CsPbBr_3$/Au	405	−3	7×10^{-4}	3.4×10^{9}	0.28	5	53
Au/$CsPbBr_3$-MPA (mp-TiO_2)/Au	405	2	20	8.9×10^{13}		1×10^{5}	54
Au/$CsPbBr_3$ QD/Au	504	10	1.9	1.3×10^{12}		3094	55
Pt/$CsPbBr_3$ QD/Pt	448	10	8.83×10^{-3}	1.4×10^{11}	2.45	7.52	This work
Pt/$CsPbBr_3$ QD-PEA/Pt			$\mathbf{149 \times 10^{-3}}$	$\mathbf{9.7 \times 10^{11}}$	**41.31**	**34.35**	
Pt/$CsPbBr_3$ QD-TCA/Pt			51.79×10^{-3}	3×10^{11}	14.34	13.90	

TCA-modified film.[51] To further analyze the role of surface ligands on the PD performance, we have measured and compared transient photoresponses at a fixed 10 V bias and under a blue LED (λ = 448 nm) light pulse with different irradiance power densities ranging from 0.2 to 50 mW cm^{-2} (Fig. S18a†). The photocurrent response is almost negligible for the control device, while it improves significantly for TCA- and PEA-treated $CsPbBr_3$ QDs-based PDs reaching a maximum photocurrent for the latter device under low light irradiance (0.2 mW cm^{-2}) (Fig. S18b†). Fig. 3b shows the photocurrent density of the PDs with increasing light irradiance power densities ranging from 0.2 to 50 mW cm^{-2}. We fitted J_{ph} *versus* incident light intensity with a power law equation ($J_{ph} \propto P^{\beta}$, where P is the light intensity and β is the recombination under illumination), which shows a sublinear relationship (Fig. S19†). In general, the power exponent β equals to 1 or very close to 1 indicates the high absorption and conversion efficiency of a high-performance PD. However, a nonunity exponent of β ($0 < \beta < 1$) is often found in LHP-based PDs due to the complex processes of charge generation, charge transportation, charge recombination, and charge trapping within the perovskite materials.[52] As seen, the value of exponent β decreases from 0.41 ± 0.009 for the PEA-treated $CsPbBr_3$ QDs to 0.37 ± 0.010 for the TCA treatment $CsPbBr_3$ QDs suggesting the existence of higher second-order charge recombination in TCA treatment $CsPbBr_3$ QDs based PDs.

Fig. 3c and d show R and EQE of these devices with a fixed 10 V bias as a function of light power. As seen, the device based on PEA-treated $CsPbBr_3$ QDs exhibits the highest values of R and EQE. The maximum R and EQE reach up to 0.149 A W^{-1} and 41.3% for PEA-treated $CsPbBr_3$ QDs-based PD compared to 0.051 A W^{-1} and 14.3% for the TCA-treated $CsPbBr_3$ QDs based PD under low irradiation of blue light (0.1 mW cm^{-2}). In addition, PEA-treated $CsPbBr_3$ QDs-based PD shows almost 3 times higher D^* (Fig. 3e) and an on/off ratio (Fig. 3f) than the TCA-treated $CsPbBr_3$ QDs-based PD, and almost 23 times higher J_{ph} than the control PD (Fig. 3b), which highlight its superior charge transfer and performance. Next, temperature-dependent photoluminescence (PL) spectroscopy was applied to determine the exciton behavior of $CsPbBr_3$ QDs-based films. As seen in Fig. S20,† modification of the shell with PEA and TCA increases the exciton binding energy of the $CsPbBr_3$ QDs, which suggests enhanced stability and absorption efficiency. On the other hand, the higher exciton binding energy can affect the charge extraction, which may affect the device's sensitivity.

Therefore, the moderate exciton binding energy of PEA-treated $CsPbBr_3$ QDs film with lower non-radiative recombination and defects helps to improve the device sensitivity. In turn, the highest exciton binding energy observed for the TCA-treated $CsPbBr_3$ QDs film with higher non-radiative recombination and defects limits its performance as compared to the PEA-treated $CsPbBr_3$ QDs film. Table 1 summarizes the performance parameters of our PDs and other previously reported photoconductor-type PDs based on $CsPbBr_3$ QDs.

Finally, the PEA-treated $CsPbBr_3$ QDs-based PD was tested by collecting photodetection data (under fixed 10 V bias and 0.2 mW cm^{-2} blue light pulse) at various bending angles and multiple cycles of bending. A custom-built setup (Fig. S21†) was used to bend the device, and photodetection data was measured during the bending of the device at every 5° angle, from 0° to 35°. The results, depicted in Fig. 4a, show that the photocurrent increases slightly with increasing the bending angle from 0 to 15° as the distance between the source and the device decreases, leading to an increase in luminescence intensity. After 15°, the photocurrent decreases as expected due to the strong bending of the PD, whereby the increasing light hits the surface at a very flat angle and is increasingly reflected there. Furthermore, the durability of the PD was measured against the bending cycles. As seen in Fig. 4b, the device has retained ~96% of its performance after a 150 bending cycle. These results reveal that both the fabric substrate and the $CsPbBr_3$ QDs-films are durable for after 150 bending cycles and long-time flexible operations. Besides the mechanical bending stability, long-term operational and environmental stability is also measured. The functional stability of unencapsulated PEA-treated $CsPbBr_3$ QDs-based PD was measured under ambient conditions (Relative humidity = 30%, 25 °C) at 10 V bias and continuous 5 mW cm^{-2} blue light pulse. As shown in Fig. 4c, the output of this PD maintained 90% of its initial performance after 10 hours of continuous operation. Next, the unencapsulated PD was kept for 2 weeks under dark condition in ambient condition (Fig. 4d). Notably, the device still maintains 93.8% of its initial performance confirming noticeable operational stability. We also tracked and compared the long-term shelf life stability of the reference and PEA-treated $CsPbBr_3$ QDs-based PDs without any encapsulation under 30–40% relative humidity at room temperature. It was observed that these conditions were detrimental for the device stability, likely due to ligand detachment from the QD surface upon aging.[27] The PEA-treated $CsPbBr_3$ QDs-based PD maintained only ~14% of its initial efficiency after aging for 4 months (Fig. S22†), while the reference device completely decomposed, showing no response under similar

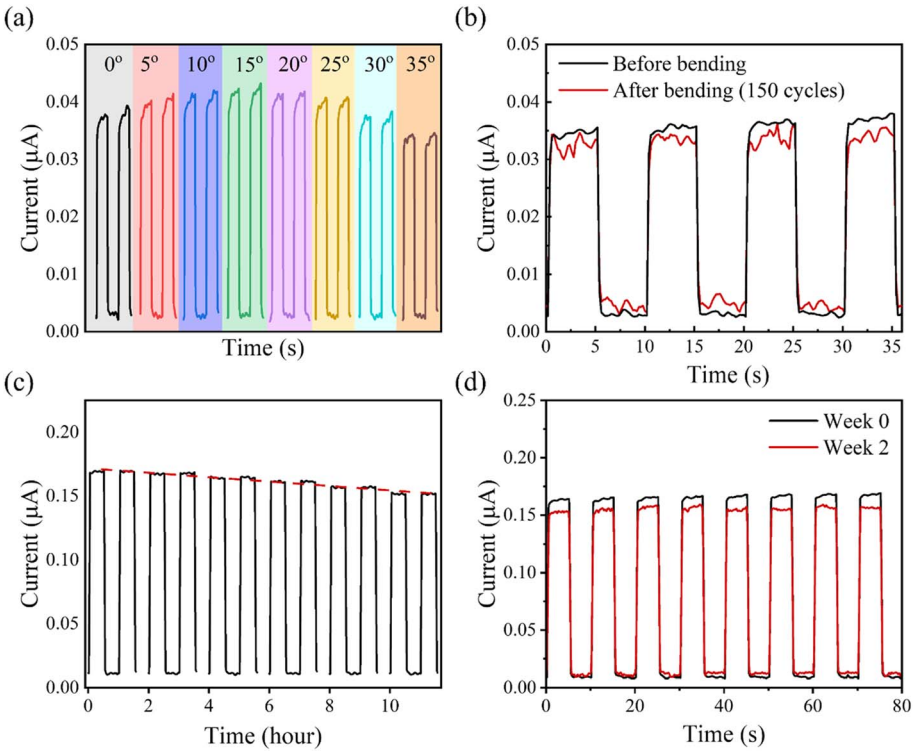

Fig. 4 Transient photocurrent (a) under different bending angles from 0° to 35° and (b) before and after 150 bending cycles under the illumination of 0.2 mW cm^{-2} of 448 nm for the PEA-treated $CsPbBr_3$ QDs-based PD. Transient photocurrent of the PEA-treated $CsPbBr_3$ QDs-based PD under the pulsed illumination of 448 nm at 10 mW cm^{-2} for (c) continuous 10 hours and (d) after storing the device under dark humid free conditions for two weeks.

conditions. Our works on developing encapsulation protocol and further rational compositional engineering of QD shell, which would allow to achieve stable and durable devices, are in progress.

3. Conclusion

In summary, we investigated the effect of surface ligand modification on the photodetection properties of $CsPbBr_3$ QDs-based PD. Specifically, the aromatic short-chain phenethylamine (PEA) and *trans*-cinnamic acid (TCA) were used as typical L- and X-type ligands. First, we analyzed the effect of the work function of the metal electrode on the transient photoresponse of the reference $CsPbBr_3$ QDs-based PD, and found that the device with platinum electrodes exhibits the best output performance. Then, individual $CsPbBr_3$ QDs with various PEA (L-type) doping concentrations were synthesized and characterized. The planar-type PD based on $CsPbBr_3$ QDs with optimum 100 μL PEA doping concentration shows the best photodetection properties of blue light at 10 V with a peak responsivity of 149 mA W^{-1} and EQE of 41.3%, which is almost 20 times higher than those of control device. The improved PD performance was attributed to the higher conductivity and average PL lifetime, lower surface defect centres, and reduction in non-radiative recombination in PEA-modified $CsPbBr_3$ QDs films. Similarly, $CsPbBr_3$ QDs-based PD treated with TCA (X-type) shows a similar improvement in performance yielding a peak responsivity of 51.8 mA W^{-1} and an EQE of 14.3%. Despite the enhanced conductivity, higher defects and second-order charge recombination, TCA-treated $CsPbBr_3$ QDs-based PD restricts its performance compared to the PEA-treated $CsPbBr_3$ QDs-based device. As verified from UPS and temperature-dependent PL spectroscopy measurements, PEA-treated $CsPbBr_3$ QDs led to a more favourable energetic match with the metal electrode and a balanced approach between exciton binding energy and lower non-radiative recombination helps to exhibit the best output performance than all other $CsPbBr_3$ QDs based photoconductor. At last, the flexibility and long-term operational tests revealed the excellent stability of PEA-treated $CsPbBr_3$ QDs PD. These findings provide great opportunities for designing flexible and wearable optoelectronic devices by fine-tuning of the QDs shell.

4. Experimental section

4.1 Materials

Cs_2CO_3 (99.995%), $PbBr_2$ (98%), toluene (99.8%, anhydrous), phenethylamine (PEA, 99%) and ethyl acetate (EA, 99.8%, anhydrous) are from Sigma Aldrich. *Trans*-cinnamic acid (TCA, 98%) from Acros organics. Tetra-*n*-octylammonium bromide (TOABr, 98%) and (di-*n*-dodecyl) dimethylammonium bromide (DDABr, 98%) are from Thermo Scientific. Octanoic Acid (99%) from Roth. All chemicals used directly without any further purification.

4.2 Textile substrate

The textile substrate used for the photodetectors layer system is a glass fiber fabric, as shown in the photograph of Fig. S12a.† The glass fiber fabric is coated by polytetrafluoroethylene (PTFE) with thicknesses between 70 μm and 250 μm. A photograph is given in Fig. S12a† and a SEM image of the surface in Fig. S12b.† From the SEM investigation it is seen, that the PTFE coating results in a closed surface without holes, voids or steep edges, which is required for short-circuit-free photodetectors. The pre-treatment experiments showed that the fabric remains stable in the vacuum at 1 mbar for at least 30 min at a temperature of 230 °C as needed for the layer deposition. In addition, the thermal expansion of the fabric with PTFE coating matches to the metal layers. So that the photodetectors layer system can be applied without cracking.

4.3 Synthesis of $CsPbBr_3$ QDs

In order to synthesize $CsPbBr_3$ QD we adopted the ambient temperature method reported in the literature.[42] For a typical procedure 3 stock solutions were prepared. Cesium octanoate (Cs-OTAc), by dissolving Cs_2CO_3 (0.5 mmol) in 10 mL of octanoic acid, $PbBr_2$-TOABr by dissolving $PbBr_2$ (0.5 mmol) and TOABr (1 mmol) in 5 mL of toluene, and DDABr (0.5 mmol) solution by dissolving in 10 mL of toluene. Next, 1 mL of Cs-OTAc was swiftly injected into the vigorously stirred $PbBr_2$-TOABr solution and stirring was continued for 20 s, followed by the addition of 1.3 mL of DDABr solution. Then EA was added to precipitate $CsPbBr_3$ QD and centrifuged at 9000 rpm for 10 min. Raw material was washed two times more by redispersing QD in toluene and precipitation by EA followed by centrifugation at the same conditions. Such prepared material was allowed to dry at room temperature and was used as a reference and for subsequent modifications.

4.4 Ligand exchange

30 mg of $CsPbBr_3$ QDs were redispersed in 5 mL of toluene in an ultrasonic bath for 5 min and the various amount of PEA (35, 70, 100 or 150 μL) or TCA (120 mg) were added. All 5 samples were then stirred in a room temperature for 2 minutes, after which they were precipitated by the addition of EA and centrifuged at 9000 rpm for 10 min. Purification procedure was subsequently applied one more time, and the obtained powders were allowed to dry naturally at room temperature.

4.5 Device fabrication and characterisation

100 nm-thick Pt/Au electrodes are deposited on the surface of the fabrics with channel width of 200 μm and channel length of 600 μm by magnetron sputtering (Leica EM MED020) with the help of a custom-made shadow mask. The QDs are deposited on the substrate by drop casting. For this, 25 mg of QDs dispersed in 1 mL toluene and 2 μL drop is put on the substrate between the electrodes. The drop allowed to dry naturally at room temperature. All dark current–voltage and PD response measurements were conducted using an SATs probe station connected to a Bio-Logic SP-150e potentiostat with two individual channels. The illumination power of the Blue LED (Luxeon Star LEDs) was optimized using the Thorlabs GmbH., PM 100D.

4.6 X-ray diffraction patterns

X-ray diffraction patterns were collected using an Empyrean diffractometer (PANalytical) with a Cu X-ray source (40 kV, 40 mA) over 10° to 50° of 2θ, with a steady sample holder. The radiation used for the measurements was Cu-KL3 ($\lambda = 1.541$ Å).

4.7 UV-visible absorption

UV-visible absorption spectra are collected using SEC2020 spectroscopic system from ALS.

Photoluminescence spectra at room temperature are taken using a Shimadzu RF-6000 spectrometer and the room-temperature TRPL data were collected using the sub-nanosecond (75 ps FWHM) pulsed diode laser with central emission wavelength 405 nm from Hamamatsu – laser – head M8903-01 and driver – picosecond light pulser C8898. The pulse repetition rate was set to 100 kHz (10 μs). For the detection we used the Andor SR-500i monochromator with diffraction grating 600/500 nm and Peltier cooled charge-coupled device (CCD) camera of Andor DV420-FI. After acquiring the PL spectrum, the central detection wavelength was tuned to the PL maximum peak, and the detection was switched from CCD camera to single photon avalanche photodiode SPAD – model SPCM-AQR-13 from Excelitas Technologies. The sync and the SPAD signals were registered using a picosecond event timer – model PicoQuant HydraHarp 400. The excitation laser light and detection PL signal were aligned in confocal setup *via* Nikon L Plan achromatic objective with ×100 magnification and 0.7 numerical aperture (NA).

The TRPL decay is fitted using a tri-exponential decay using the following formula;

$$y(t) = y(0) + A_1 e^{-\frac{t}{\tau_1}} + A_2 e^{-\frac{t}{\tau_2}} + A_3 e^{-\frac{t}{\tau_3}}$$

The average lifetimes are calculated using the intensity average formula;

$$\tau_{avg} = \frac{\sum_{i=1}^{n} A_i \tau_i^2}{\sum_{i=1}^{n} A_i \tau_i}$$

4.8 Temperature dependent photoluminescence

Temperature dependent photoluminescence spectra were measured under laser excitation of 405 nm (3.06 eV) on samples placed on a cold finger of a continuous flow cryostat. The excitation light was focused by means of a 50 long-working distance objective with a 0.55 numerical aperture (NA) producing a spot of about 1 mm diameter. The signal was collected *via* the same microscope objective (the backscattering geometry), sent through a 0.75 m SpectraPro HRS monochromator from the Princeton Instruments, and detected by

using a liquid nitrogen cooled charge-coupled device (CCD) Pylon camera from the Princeton Instruments.

4.9 Ultraviolet photoelectron spectroscopy

Ultraviolet photoelectron spectroscopy measurements of the films were collected with a UPS unit integrated into the PHI 5000 VersaProbe XPS system. The HOMO and LUMO levels were calculated from:

$$\text{HOMO} = 21.22 - (E_{\text{cutoff}} - E_{\text{onset}})$$

$$\text{LUMO} = \text{HOMO} + \text{Bandgap}$$

4.10 TEM system

TEM system is a HT7820 from the Hitachi company (Hitachi High-Tech Corporation, Tokyo, Japan). It is equipped with a tungsten filament. The main camera is a XAROSA (30 frames per second, 20 Megapixel) from the Emsis company (EMSIS GmbH, Münster, Germany). For the evaluation the software EMIP-EX was used (Hitachi, Vers. 07.21). Only square particles were measured. Most of the micrographs were taken at 100 keV electron energy. About 1 mg of each sort of $CsPbBr_3$ QDs were dissolved in 1 mL toluene under sonication for 30 min, respectively. The suspensions were drop casted on the TEM grids covered by a carbon film, and dried in air, respectively.

Data availability

The data that support the findings of this study are available in the ESI† of this article.

Author contributions

D. P. conceived the idea. J. N. synthesized and characterized the $CsPbBr_3$ QDs. V. A. and A. M. fabricated the films and devices and performed photodetection studies. G. J. and J. D. did the TEM measurement and analysis. P. B. performed NMR measurements. G., M. R., A. K. and M. R. M. performed TRPL and PL temperature dependence measurements and analysis. B. D.-I. and J. P. participated in the manuscript discussion. S. A. performed UPS. P. Y., A. M. and D. P. analyzed all the data. A. M. wrote the first draft of the manuscript. D. P. performed the manuscript revision and supervised this project. All authors discussed the results and commented on the manuscript.

Conflicts of interest

The authors declare no conflict of interest.

Acknowledgements

J. N. and V. A. contributed equally to this work. J. N. and D. P. acknowledge the National Centre for Research and Development (V4-JAPAN/2/14/PeDET/2022) for financial support.

References

1 Y. Xu and Q. Lin, *Appl. Phys. Rev.*, 2020, **7**, 011315.
2 H. Wu, Y. Ge, G. Niu and J. Tang, *Matter*, 2021, **4**, 144–163.
3 C. Wang, X. Zhang and W. Hu, *Chem. Soc. Rev.*, 2020, **49**, 653–670.
4 E. O. Polat, G. Mercier, I. Nikitskiy, E. Puma, T. Galan, S. Gupta, M. Montagut, J. J. Piqueras, M. Bouwens, T. Durduran, G. Konstantatos, S. Goossens and F. Koppens, *Sci. Adv.*, 2019, **5**, eaaw7846.
5 P. C. Y. Chow and T. Someya, *Adv. Mater.*, 2020, **32**, 1902045.
6 L. Li, S. Ye, J. Qu, F. Zhou, J. Song and G. Shen, *Small*, 2021, **17**, 2005606.
7 R. D. Jansen-van Vuuren, A. Armin, A. K. Pandey, P. L. Burn and P. Meredith, *Adv. Mater.*, 2016, **28**, 4766–4802.
8 C. Bao, J. Yang, S. Bai, W. Xu, Z. Yan, Q. Xu, J. Liu, W. Zhang and F. Gao, *Adv. Mater.*, 2018, **30**, 1803422.
9 X. Bai, W. Gao, Y. Cai, Z. Bai, Y. Qi, B. Yan, Y. Wang, Z. Lu and J. Ding, *Chem.–Eur. J.*, 2023, **29**, e202203022.
10 J. Plentz, G. Andrä, T. Pliewischkies, U. Brückner, B. Eisenhawer and F. Falk, *Mater. Sci. Eng., B*, 2016, **204**, 34–37.
11 A. Gawlik, U. Brückner, G. Schmidl, V. Wagner, W. Paa and J. Plentz, *Materials*, 2023, **16**, 4841.
12 A. K. Jena, A. Kulkarni and T. Miyasaka, *Chem. Rev.*, 2019, **119**, 3036–3103.
13 Y. Liu, Y. Zhang, Z. Yang, J. Feng, Z. Xu, Q. Li, M. Hu, H. Ye, X. Zhang, M. Liu, K. Zhao and S. Liu, *Mater. Today*, 2019, **22**, 67–75.
14 L. Sun, W. Li, W. Zhu and Z. Chen, *J. Mater. Chem. C*, 2020, **8**, 11664–11674.
15 M. García-Batlle, W. Zia, C. A. Aranda, M. Saliba, O. Almora, A. Guerrero and G. Garcia-Belmonte, *Sol. RRL*, 2022, **6**, 2200173.
16 A. Mahapatra, V. Anilkumar, R. D. Chavan, P. Yadav and D. Prochowicz, *ACS Photonics*, 2023, **10**, 1424–1433.
17 Y. Zhang, Y. Liu and S. Frank) Liu, *Adv. Funct. Mater.*, 2023, **33**, 2210335.
18 V. Anilkumar, A. Mahapatra, J. Nawrocki, R. D. Chavan, P. Yadav and D. Prochowicz, *Adv. Opt. Mater.*, 2024, **12**, 2302032.
19 Z. Yang, Y. Deng, X. Zhang, S. Wang, H. Chen, S. Yang, J. Khurgin, N. X. Fang, X. Zhang and R. Ma, *Adv. Mater.*, 2018, **30**, 1704333.
20 G. Li, Y. Wang, L. Huang and W. Sun, *ACS Appl. Electron. Mater.*, 2022, **4**, 1485–1505.
21 C. Perumal Veeramalai, S. Yang, R. Zhi, M. Sulaman, M. I. Saleem, Y. Cui, Y. Tang, Y. Jiang, L. Tang and B. Zou, *Adv. Opt. Mater.*, 2020, **8**, 2000215.
22 C. Bi, S. V. Kershaw, A. L. Rogach and J. Tian, *Adv. Funct. Mater.*, 2019, **29**, 1902446.
23 T. Yang, F. Li and R. Zheng, *ACS Appl. Electron. Mater.*, 2019, **1**, 1348–1366.
24 K. Shen, H. Xu, X. Li, J. Guo, S. Sathasivam, M. Wang, A. Ren, K. L. Choy, I. P. Parkin, Z. Guo and J. Wu, *Adv. Mater.*, 2020, **32**, 2000004.

25 H. Wang, Z. Du, X. Jiang, S. Cao, B. Zou, J. Zheng and J. Zhao, *ACS Appl. Mater. Interfaces*, 2024, **16**, 11694–11703.
26 D. Liu, Y. Guo, M. Que, X. Yin, J. Liu, H. Xie, C. Zhang and W. Que, *Mater. Adv.*, 2021, **2**, 856–879.
27 N. Fiuza-Maneiro, K. Sun, I. López-Fernández, S. Gómez-Graña, P. Müller-Buschbaum and L. Polavarapu, *ACS Energy Lett.*, 2023, **8**, 1152–1191.
28 P. Ramasamy, D.-H. Lim, B. Kim, S.-H. Lee, M.-S. Lee and J.-S. Lee, *Chem. Commun.*, 2016, **52**, 2067–2070.
29 L. Zhou, K. Yu, F. Yang, J. Zheng, Y. Zuo, C. Li, B. Cheng and Q. Wang, *Dalton Trans.*, 2017, **46**, 1766–1769.
30 A. Surendran, X. Yu, R. Begum, Y. Tao, Q. J. Wang and W. L. Leong, *ACS Appl. Mater. Interfaces*, 2019, **11**, 27064–27072.
31 X. Feng, Z. He, W. Zhu, M. Zhao, Z. Liu, S. Yang, S. Tang, Q. Guo, Z. Jin, D. Chen, G. Ding and G. Wang, *J. Mater. Chem. C*, 2021, **9**, 609–619.
32 M. Gong, R. Sakidja, R. Goul, D. Ewing, M. Casper, A. Stramel, A. Elliot and J. Z. Wu, *ACS Nano*, 2019, **13**, 1772–1783.
33 E. T. Vickers, T. A. Graham, A. H. Chowdhury, B. Bahrami, B. W. Dreskin, S. Lindley, S. B. Naghadeh, Q. Qiao and J. Z. Zhang, *ACS Energy Lett.*, 2018, **3**, 2931–2939.
34 H. Wang, Y. Dou, P. Shen, L. Kong, H. Yuan, Y. Luo, X. Zhang and X. Yang, *Small*, 2020, **16**, 2001062.
35 W. Yan, J. Shen, Y. Zhu, Y. Gong, J. Zhu, Z. Wen and C. Li, *Nano Res.*, 2021, **14**, 4038–4045.
36 L. Ruan, W. Shen, A. Wang, Q. Zhou, H. Zhang and Z. Deng, *Nanoscale*, 2017, **9**, 7252–7259.
37 M. A. Uddin, J. K. Mobley, A. A. Masud, T. Liu, R. L. Calabro, D.-Y. Kim, C. I. Richards and K. R. Graham, *J. Phys. Chem. C*, 2019, **123**, 18103–18112.
38 D. Yang, X. Li, W. Zhou, S. Zhang, C. Meng, Y. Wu, Y. Wang and H. Zeng, *Adv. Mater.*, 2019, **31**, 1900767.
39 V. G. V. Dutt, S. Akhil, R. Singh, M. Palabathuni and N. Mishra, *J. Phys. Chem. C*, 2022, **126**, 9502–9508.
40 M. L. H. Green, *J. Organomet. Chem.*, 1995, **500**, 127–148.
41 C. K. Ng, W. Yin, H. Li and J. J. Jasieniak, *Nanoscale*, 2020, **12**, 4859–4867.
42 Y. Liu, S. Tang, J. Fan, E. Gracia-Espino, J. Yang, X. Liu, S. Kera, M. Fahlman, C. Larsen, T. Wågberg, L. Edman and J. Wang, *ACS Appl. Nano Mater.*, 2021, **4**, 1162–1174.
43 Y.-F. Xu, M.-Z. Yang, B.-X. Chen, X.-D. Wang, H.-Y. Chen, D.-B. Kuang and C.-Y. Su, *J. Am. Chem. Soc.*, 2017, **139**, 5660–5663.
44 Y. Chen, S. R. Smock, A. H. Flintgruber, F. A. Perras, R. L. Brutchey and A. J. Rossini, *J. Am. Chem. Soc.*, 2020, **142**, 6117–6127.
45 L. Clinckemalie, D. Valli, M. B. J. Roeffaers, J. Hofkens, B. Pradhan and E. Debroye, *ACS Energy Lett.*, 2021, **6**, 1290–1314.
46 X. Liu, Z. Liu, J. Li, X. Tan, B. Sun, H. Fang, S. Xi, T. Shi, Z. Tang and G. Liao, *J. Mater. Chem. C*, 2020, **8**, 3337–3350.
47 A. Jäckel, M. L. Hupfer, E. Castro-Camus, D. M. Mittleman, G. Schmidl, A. Gawlik, J. Plentz and M. Koch, *Sci. Rep.*, 2024, **14**, 22029.
48 G. Li, J. Huang, H. Zhu, Y. Li, J.-X. Tang and Y. Jiang, *Chem. Mater.*, 2018, **30**, 6099–6107.
49 R. K. Gunasekaran, J. Jung, S. W. Yang, J. Yun, Y. Yun, D. Vidyasagar, W. C. Choi, C. Lee, J. H. Noh, D. H. Kim and S. Lee, *InfoMat*, 2023, **5**, e12393.
50 C. Bi, S. V. Kershaw, A. L. Rogach and J. Tian, *Adv. Funct. Mater.*, 2019, **29**, 1902446.
51 A. Mahapatra, D. Prochowicz, J. Kruszyńska, S. Satapathi, S. Akin, H. Kumari, P. Kumar, Z. Fazel, M. Mahdi Tavakoli and P. Yadav, *J. Mater. Chem. C*, 2021, **9**, 15189–15200.
52 A. Mahapatra, V. Anilkumar, J. Nawrocki, S. V. Pandey, R. D. Chavan, P. Yadav and D. Prochowicz, *Adv. Elect. Mater.*, 2023, **9**, 2300226.
53 M. K. Kim, Z. Munkhsaikhan, S. G. Han, S. M. Park, H. Jin, J. Cha, S. J. Yang, J. Seo, H. S. Lee, C.-J. Choi and M. Kim, *J. Mater. Chem. C*, 2022, **10**, 11401–11411.
54 L. Zhou, K. Yu, F. Yang, H. Cong, N. Wang, J. Zheng, Y. Zuo, C. Li, B. Cheng and Q. Wang, *J. Mater. Chem. C*, 2017, **5**, 6224–6233.
55 L. Pang, Y. Yao, Q. Wang, X. Zhang, Z. Jin and S. (Frank) Liu, *Part. Part. Syst. Charact.*, 2018, **35**, 1700363.